Proceedings of the 21st ICSMGE, Vienna, Austria, 14 – 19 June 2026. Pistrol, Adam & Schweiger (eds.)
Published by: ÖGG, Austrian Society for Geomechanics, Salzburg, Austria, ISBN 978-3-9503898-4-5
https://doi.org/10.53243/ICSMGE2026-1788

Comparative Assessment of Constitutive Models for Hydrate-bearing Sediments using Triaxial Compression Experiments

Mahima S Rao*, Sahil Wani, Ramesh Kannan Kandasami
*Department of Civil Engineering, Indian Institute of Technology Madras, Tamil Nadu, India, *5mahimasrao5@gmail.com*

ABSTRACT: Safe extraction of methane gas from hydrate-bearing sediments (HBS) relies on comprehensive understanding of its geomechanical behavior. Various researchers have proposed constitutive models to predict the geomechanical behavior of HBS. These models exhibit several advantages and limitations in predicting different aspects of the material response, including contraction, dilation, stiffness, failure strength, and pore pressure of HBS, across different strain levels. Therefore, it is essential to evaluate the efficacy of these models before adopting them in any coupled numerical solvers for solving boundary value problems pertaining to gas extraction. In this study, three constitutive models: Modified methane hydrate Mohr-Coulomb (MHMC) model, methane hydrate critical state (MHCS) model, and hypoplastic model, are evaluated for their capabilities in predicting HBS response. The material parameters for these models are derived from triaxial experiments conducted on laboratory-synthesized hydrate-bearing specimens with two distinct hydrate pore morphologies: grain-cementing and non-cementing. The performance of the constitutive models is assessed by comparing their response with experimental results through absolute error metrics. Although all three models adequately captured peak deviatoric stress of cemented hydrate specimens, significant differences emerged in post-peak and volumetric responses. The hypoplastic model outperformed the others by accurately replicating post-peak strain softening and volumetric deformation across both hydrate pore morphologies. The MHCS model is able to reproduce softening and dilative behavior in cemented specimens but required recalibration to account for changes in hydrate pore morphology. The MHMC model failed to capture post-peak softening and the influence of hydrate pore morphology. Further, to understand the influence of hydrate pore morphology on geomechanical behavior of HBS, parametric analysis has been carried using hypoplastic model. Overall, the study underscores the importance of incorporating hydrate pore morphology and strain degradation mechanisms within the constitutive frameworks and highlights that the hypoplastic model is a promising tool for realistic geomechanical modeling of HBS.

KEYWORDS: Geomechanical response, Elastoplastic models, Critical state, Hypoplastic models, Hydrate pore morphology.

1 INTRODUCTION

Gas hydrates are crystalline compounds composed of gas molecules encapsulated within a lattice of water molecules, formed under high-pressure and low-temperature conditions (Sloan & Koh 2007). Hydrates occur naturally in deep marine sediments and permafrost regions which are considered as one of the major sources of unconventional energy (Wani et al. 2023). However, gas extraction from hydrate-bearing sediments (HBS) by hydrate dissociation, induces alterations in the pore structure and leads to reduction in sediment strength and stiffness (Wu et al. 2020). This triggers geomechanical instabilities such as subsidence, slope failure, and other hazards. Hence, a comprehensive understanding of the geomechanical response of HBS is vital to ensure the stability and safety during production operations.

The geomechanical response of these sediments is strongly influenced by the amount of hydrate present and their pattern of accumulation within the pore structure. Depending on the formation conditions, hydrates can exhibit various morphological forms; acting as cement between grains, occupying pore spaces without bonding, or forming bridges across particles (Lijith et al. 2019). These morphologies, together with the volume of hydrate present, play a key role in governing the strength, stiffness, and deformation characteristics of the sediment (Priest et al. 2009). Therefore, accurately characterizing both hydrate pore morphology and their distribution is essential for evaluating the mechanical stability of HBS.

Several experimental studies (Hyodo et al. 2013; Masui et al. 2006) have demonstrated that increasing hydrate saturation (the ratio of hydrate volume to pore volume) enhances the shear strength of the sediment. Higher hydrate saturation is associated with a linear rise in failure shear strength and a proportional increase in the secant modulus (Zhang et al. 2015; Zhao et al. 2022). Cohesion has been observed to increase exponentially with hydrate saturation (Liu et al. 2013). However, findings regarding the angle of internal friction are less consistent. While some studies report a slight reduction in friction angle with increasing hydrate saturation (Liu et al. 2013), others suggest negligible or even opposite trends (Santamarina et al. 2015), indicating that the effect may depend on factors such as hydrate pore morphology, soil type, and testing conditions. Further, experimental studies (Rao et al. 2025) have shown that pore-filling hydrates, which predominantly occupy void spaces, offer limited mechanical reinforcement to HBS. In such configurations, the soil skeleton bears the majority of the deviatoric stress, resulting in a minimal contribution from hydrates to the strength of the sediment. Conversely, when hydrates exist as cementing or load-bearing morphologies**,** they effectively bond or bridge soil particles, thereby participating in stress transfer and significantly enhancing the overall strength and stiffness of the HBS matrix (Rao et al. 2025; Zeng et al. 2023).

In addition to experimental studies, several efforts have been made over the years to model the geomechanical behavior of HBS using different constitutive frameworks. These include nonlinear elastic models (Miyazaki et al. 2012; Wani et al. 2024), elastic perfectly plastic models (Klar et al. 2010; Pinkert & Grozic 2014), critical state-based models (Uchida et al. 2012; Gai & Sánchez 2017; De La Fuente et al. 2020; Wani & Kandasami 2025), and hypoplastic models (Zhang et al. 2018; Wani et al. 2025a). Klar et al. (2010) and Pinkert & Grozic (2014) considered the effect of hydrate saturation on cohesion, dilation angle, and stiffness while proposing a Mohr–Coulomb based model for hydrates. Further, Uchida et al. (2012), Gai & Sánchez (2017) and De La Fuente et al. (2020) considered critical state concepts to model the response of HBS incorporating the effect of hydrate saturation and the bond degradation. Recently, Wani & Kandasami (2025) incorporated the effect of pore pressure and temperature into the HISS MH model (Gai & Sánchez 2017). Some of the more recent developments also consider the role of hydrate pore-scale morphology by including a cementation coefficient to better represent the hydrate-soil interaction (Wani et al. 2025a). However, before implementing any of these constitutive models in the coupled numerical solvers to critically analyze boundary value problems, it is important to evaluate their performance particularly in predicting the strength, stiffness, and volume change behavior under different loading conditions.

In the present study, a series of experiments are conducted on both the host sand and hydrate-bearing specimens exhibiting cemented and non-cemented hydrate pore morphologies. Based on the experimental results, three constitutive models, namely the modified methane hydrate Mohr–Coulomb model (Pinkert & Grozic, 2014), the methane hydrate critical state model (Uchida et al., 2012), and the hypoplastic model for methane hydrate-bearing sediments (Wani et al., 2025a) are calibrated. These models are selected as they represent distinct theoretical frameworks such as elastic-perfectly plastic, elastoplastic based on critical state framework, and hypoplastic respectively. This selection enables a comprehensive evaluation of framework dependent capabilities in reproducing geomechanical characteristics of HBS. The predictive capabilities of these models are evaluated by comparing their predictions with experimental results.

2 MATERIALS AND METHODOLOGY

2.1 *Experimental testing*

A series of consolidated drained triaxial compression experiments are carried out using an advanced high-pressure, temperature, and gas-controlled triaxial testing equipment (Rao et al. 2024). The host sand used for hydrate formation is a poorly graded sand with a mean particle diameter of 0.28 mm, a coefficient of uniformity of 2.53, and a coefficient of curvature of 1.30. The minimum and maximum void ratios are 0.59 and 0.84, respectively. Cylindrical specimens with a diameter of 5 cm and height of 10 cm are prepared by tamping in eight layers to achieve a target porosity of 40%. Methane hydrates are synthesized using high-purity methane gas (99.99%) under pore pressure and temperature conditions of 5.25 MPa and 2 °C. To achieve cementing and non-cementing hydrate pore morphologies, the excess gas and excess water method of forming hydrates are adopted, following the procedure described in Rao et al. (2025). A hydrate saturation (S_h) of 40% is targeted. Triaxial experiments are performed on the host sand (HS) at three different effective confining pressures (σ_3' = 0.5, 1, and 2 MPa) while the methane hydrate-bearing specimens (MHBS) are sheared under an effective confining pressure of 1 MPa, at a constant axial strain rate of 0.1 mm/min.

2.2 *Constitutive modelling*

The present study employs three constitutive models for gas hydrate-bearing sediments: (i) a non-linear, elastic-perfectly plastic, modified methane hydrate Mohr–Coulomb (MHMC) model (Pinkert & Grozic 2014), (ii) an elastoplastic model based on critical state framework (Uchida et al. 2012), and (iii) a hypoplastic model (Wani et al. 2025a).

In the model proposed by Pinkert & Grozic (2014), the classical Mohr–Coulomb failure criterion with non-associated flow rule is extended by modifying the internal friction angle ($\emptyset$) and cohesion (c) to introduce nonlinearity into the stress–strain response. The effects of gas hydrate inclusion are captured by adjusting the cohesion, dilation angle (ψ), and elastic modulus (E). The governing equations of the model are presented in Equation (1) to (6). In this formulation, f and g are yield and plastic potential function respectively. σ_1' and σ_3' are the major and minor effective principal stresses. α is a scaling constant ranging from 0 to 1, and γ_p^f denotes a portion of the plastic shear strain γ_p. $\emptyset_{max}$ represents the maximum internal friction angle, while σ_t' is a constant with unit of pressure. γ is the total shear strain. $a_1,\ a_2,\ a_3,\ \delta_1,\ \delta_2,\ \delta_3,\ \delta_4, e_1,\ e_2$ and e_3 are model-specific constants. The specific parameter values used to calibrate this model using the experimental results obtained in the current study are provided in Table 1.

$$f = \sigma_1' - \sigma_3' \frac{1+sin\emptyset}{1-sin\emptyset} - 2c\sqrt{\frac{1+sin\emptyset}{1-sin\emptyset}} \quad (1)$$

$$g = \sigma_1' - \sigma_3' \frac{1+sin\psi}{1-sin\psi} \quad (2)$$

$$sin\emptyset = \left[\alpha + (1-\alpha)\left(\frac{2\sqrt{\gamma_p \gamma_p^f}}{\gamma_p^f + \gamma_p}\right)\right] sin\emptyset_{max} \quad (3)$$

$$c = a_1(1 - e^{-\sigma_3'/\sigma_t'}) + a_2 s_h^{a_3} \quad (4)$$

$$\sin\psi = \sin\left(\delta_1 - \delta_2 \ln\left(\frac{\sigma_3'}{1\ \text{MPa}}\right)\right) + \delta_3 s_h (1 - e^{-\gamma/\delta_4}) \quad (5)$$

$$E = e_1\left(\frac{\sigma_3'}{1\ \text{MPa}}\right)^{e_2} + e_3 s_h \quad (6)$$

Table 1. Model parameters used for the calibration of MHMC model.

Parameter	Value	Unit	Parameter	Value	Unit
α	0.2	-	δ_1	0.005	-
γ_p^f	9	%	δ_2	0.131	-
$\emptyset_{max}$	30.77	deg	δ_3	0.07	-
a_1	0.010	MPa	δ_4	0.043	-
a_2	2.060	MPa	e_1	500	MPa
a_3	1.096	-	e_2	2.69	-
σ_t'	0.490	MPa	e_3	932	MPa

The methane hydrate critical state (MHCS) model, proposed by Uchida et al. (2012), is based on the Modified Cam-Clay framework considering associated flow rule. The influence of gas hydrates on sediment behavior particularly cementation and dilatation are incorporated through two additional terms in the yield function (f): p_{cc}' and p_{cd}', as shown in Equation (7). These terms account for the progressive degradation of hydrate-induced cementation with increasing plastic strain. To ensure a smooth transition from elastic to plastic behavior, the model introduces a sub-loading surface concept governed by a sub-loading ratio R. The complete set of equations defining the MHCS model is provided in Equations (7) to (14). q is the deviatoric stress, p' is the mean effective stress, and p_{cs}' is the pre-consolidation stress. M is the slope of the critical state line in p'- q space, representing the critical state stress ratio. S_h^{mec} is the mechanical hydrate saturation and χ is the degradation factor. $d\epsilon_d^p$ is the plastic deviatoric strain increment. $d\epsilon^p$ is the plastic strain increment. $\nu,\ \kappa,$ and η are the specific volume, slope of swelling line, and Poisson's ratio respectively. λ and N are slope and intercept of normal compression line. K' and G_{hs} are bulk and shear modulus of hydrate-bearing soils respectively. $\zeta_1,\ \zeta_2,\ \zeta_3,\ \zeta_4,\ m,\ u$ and m_2 are material constants. The values of the parameters used to calibrate the MHCS model using the triaxial compression experiments are listed in Table 2.

$$f = q^2 + M^2(p' + p_{cc}')[p' - R(p_{cs}' + p_{cd}' + p_{cc}')] \quad (7)$$

$$p_{cd}' = \zeta_1 (S_h^{mec})^{\zeta_2} \quad (8)$$

$$p_{cc}' = \zeta_3 (S_h^{mec})^{\zeta_4} \quad (9)$$

$$S_h^{mec} = \chi s_h \quad (10)$$

$$d\chi = -m\chi d\epsilon_d^p (0 \le \chi \le 1) \quad (11)$$

$$dR = -u\left(\frac{1 + (p'_{cd} + p'_{cc})}{p'_{cs}}\right)\ln R|d\epsilon^p| \tag{12}$$

$$K' = \frac{\nu}{\kappa}p' \tag{13}$$

$$G_{hs} = 3K'\frac{1-2\eta}{2(1+\eta)} + m_2 S_h^{mec} \tag{14}$$

Table 2. Model parameters used for calibration of the MHCS model.

Parameter	Value	Unit	Parameter	Value	Unit
M	0.96	-	ζ_1	42	MPa
λ	0.16	-	ζ_2	1.6	-
κ	0.012	-	ζ_3	0.1	MPa
N	1.6536	-	ζ_4	1	-
ν	1.67	-	m	1	-
p'_{cs}	5	MPa	m_2	1000	MPa
η	0.3	-	u	15	-

The hypoplastic model (Wani et al. 2025a) employed in this study is modified form of the extended MS-IS hypoplastic framework (Wani et al. 2025b). The model incorporates both the intergranular strain (IS) mechanism and a memory surface (MS), along with a stiffness degradation factor, to simulate the evolving behavior of HBS. The model formulations are provided in Equations (15) to (22). The Jaumann stress rate ($\overset{\circ}{\boldsymbol{\sigma}}$) is formulated as a function of both soil and hydrate related components. The parameters c_1, c_2, c_3, and c_4 represent the primary hypoplastic material constants, while $\dot{\boldsymbol{\varepsilon}}$ denotes the strain rate and $\boldsymbol{\sigma}^*$ is the deviatoric stress. I_s is stiffness function defined in Equation (16), that depends on the current void ratio e and hydrate saturation S_h. f_b is 1 for triaxial condition, and β_{I_s} is a model parameter. The scalar quantity r is derived from the deviatoric stress and trace of the stress tensor. The critical void ratio e_{cr} determined using Equation (17), is based on parameters e_{c0} (intercept of critical state line), atmospheric pressure p_a, and Cauchy stress $\boldsymbol{\sigma}$, with Γ and ω governing the slope of the critical state line. Hydrate-related effects such as densification and bonding are captured through functions $h(S_h)$ and $j(S_h)$, expressed in Equations (18) and (19), and defined by material constants ψ_1, ψ_2, ψ_3 and k_h. The identity tensor is denoted as $\boldsymbol{I}$, and l refers to the phase length parameter. The term $\boldsymbol{g}(S_h)$, given in Equation (20), accounts for pseudo-cohesion due to hydrates and is defined using parameters a, b, and the cementation coefficient α_h which is governed by hydrate pore morphology. α_h degrades with strain as shown in Equation (21) controlled by a degradation rate parameter n. The density function I_e, introduced in Equation (22), modifies the stress response in relation to e_{cr}, with α_{I_e} controlling the degree of strain softening. The list of model parameters used for calibrating the hypoplastic model is given in Table 3. α_h values are considered to be 0.5 and 0.9 for non-cementing and cementing hydrate specimens respectively as mentioned in Wani et al. (2025a).

$$\overset{\circ}{\boldsymbol{\sigma}} = I_s\left(\begin{array}{c} c_1 tr(\boldsymbol{\sigma})\dot{\boldsymbol{\varepsilon}} + c_2\frac{tr(\boldsymbol{\sigma}\dot{\boldsymbol{\varepsilon}})\boldsymbol{\sigma}}{tr(\boldsymbol{\sigma})} + \\ + \left(c_3\frac{\boldsymbol{\sigma}^2}{tr(\boldsymbol{\sigma})} + c_4\frac{\boldsymbol{\sigma}^{*2}}{tr(\boldsymbol{\sigma})}\right)\| \dot{\boldsymbol{\varepsilon}} \| I_e \end{array}\right) - \boldsymbol{g}(S_h) \tag{15}$$

$$I_s = f_b \exp\frac{\beta_{I_s}(e_{cr} - e)}{(1+r)^2} \tag{16}$$

$$e_{cr} = (e_{c0} + h(S_h))\exp\left(-\Gamma\left(\frac{\mathrm{tr}(\boldsymbol{\sigma})}{p_a}\right)^{\omega}\right) + j(S_h) \tag{17}$$

$$h(S_h) = \left(\psi_1 \times l^{\psi_3}\right)S_h^{\psi_2} \tag{18}$$

$$j(S_h) = k_h\sqrt{\frac{-\mathrm{tr}\left(\boldsymbol{g}(S_h)\right)}{-\mathrm{tr}\left(\boldsymbol{g}(S_h)\right) + \mathrm{tr}\,(\boldsymbol{\sigma})}} \tag{19}$$

$$\boldsymbol{g}(S_h) = (a(\alpha_h S_h)^b \times l)\boldsymbol{I} \tag{20}$$

$$\dot{\alpha_h} = -n\alpha_h\|\dot{\boldsymbol{\varepsilon}}\| \tag{21}$$

$$I_e = \left(\frac{e}{e_{cr}}\right)^{\alpha_{I_e}} \tag{22}$$

Table 3. Model parameters used for calibration of the hypoplastic model.

Parameter	Value	Unit	Parameter	Value	Unit
c_1	-50.5	-	β_{I_s}	3.5	-
c_2	-567.95	-	ψ_1	0.874	-
c_3	-404.88	-	ψ_2	3	-
c_4	51.98	-	ψ_3	0.281	-
e_{c0}	0.84	-	k_h	1.2	-
Γ	0.11	-	n	8	-
ω	0.4	-	a	165.63	MPa
α_{I_e}	0.25	-	b	1.8	-

3 RESULTS AND DISCUSSIONS

The results obtained from the consolidated drained triaxial compression experiments are utilized for the comparison of responses of constitutive models considered in this study. Figure 1 presents the deviatoric stress (q) and volumetric strain (ε_v) responses with axial strain (ε_a) for the host sand specimens subjected to effective confining pressures of 0.5, 1, and 2 MPa. An increase in effective confinement pressure led to a corresponding rise in the peak deviatoric stress. Furthermore, the post-peak behavior exhibited a transition from marginal strain-softening at lower confinement pressure to strain-hardening at higher confinement pressure. A similar trend is observed in volumetric response, which shifted from dilation to contraction with increasing effective confining pressure.

Figure 1 also includes model predictions from the three constitutive frameworks. Overall, the models are able to reasonably capture both the stress–strain and volumetric strain behavior across the range of confining pressures. Notably, the models replicated the observed volumetric transition from dilation to contraction. However, some discrepancies are identified, particularly in the prediction of value of the volumetric strains and initial stiffness. For instance, the MHMC model underpredicts the initial tangent stiffness by approximately 28.9% at σ_3' = 0.5 MPa, while significantly overpredicting it by a factor of 4.5 at σ_3' = 2 MPa. In terms of peak deviatoric stress, the same model shows an underprediction of 8.7% at σ_3' = 0.5 MPa and an overprediction of 14% at σ_3' = 2 MPa. Similarly, the MHCS model overestimates the peak deviatoric stress by 31.5% under a confinement of σ_3' = 0.5 MPa.

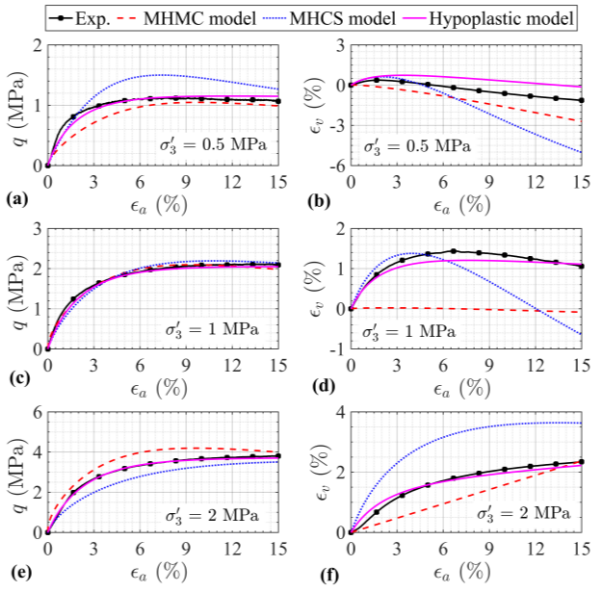

Figure 1. Plot of deviatoric stress and volumetric deformation with axial strain for HS.

To further assess and compare the predictive capabilities of the three constitutive models, box plots are plotted for the absolute error $|e|$ in predicted deviatoric stress and volumetric strain across different effective confining pressures (0.5, 1, and 2 MPa), as illustrated in Figure 2. The analysis of the box plots indicates that the MHMC model and MHCS model exhibit greater sensitivity to changes in effective confinement pressure. This is evident from the larger interquartile ranges (IQRs) and the shifting of medians away from zero, particularly at $\sigma_3{}' = 0.5$ and 2 MPa, whereas the deviations are narrower and centered around zero at $\sigma_3{}' = 1$ MPa. In contrast, the hypoplastic model demonstrates consistently narrow IQRs with medians close to zero across all effective confinement stresses, indicating better performance.

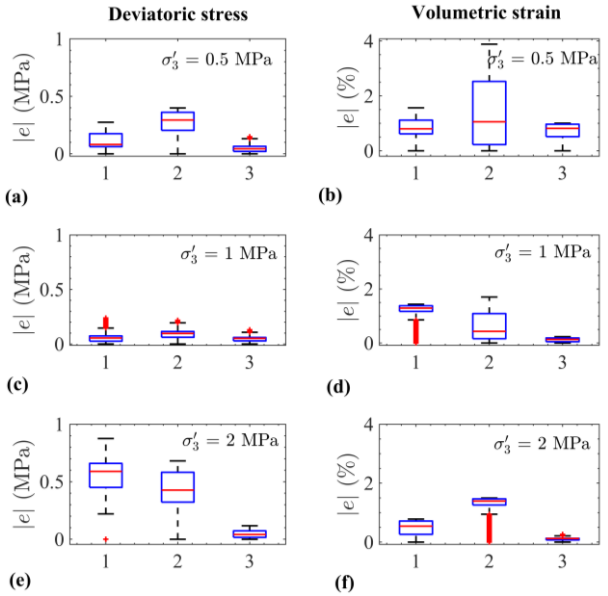

Figure 2. Comparison of absolute error in predicted q and ε_v by 1. MHMC model, 2. MHCS model and 3. Hypoplastic model for HS at different $\sigma_3{}'$.

The stress–strain and volumetric strain responses of MHBS with 40% hydrate saturation and cemented morphology, tested under an effective confining pressure of 1 MPa is presented in Figure 3(a) and (b). Experimental results reveal a pronounced increase in initial tangent stiffness (4.1 times), and peak deviatoric stress (2.2 times) compared to the host sand at 1 MPa effective confinement pressure. Additionally, it exhibited predominant post-peak strain-softening, and volumetric dilation compared to HS. The distinct strain softening observed in the cemented hydrate specimens is indicative of progressive degradation of hydrate induced cementation bonds.

To evaluate the capability of the constitutive models in capturing the complex mechanical behavior of hydrate-bearing specimen with cemented morphology, the predicted stress–strain and volumetric deformation responses from all three models are compared against experimental results as shown in Figure 3. Both the MHCS model and the hypoplastic model incorporate degradation mechanisms through the degradation parameter χ and cementation coefficient degradation ($\dot{\alpha_h}$) respectively, which allow model to effectively replicate the pronounced post-peak strain-softening observed in the experimental data. This feature is critical in representing the progressive breakdown of hydrate cementation bonds under continued shearing. In contrast, the MHMC model, which lacks such degradation mechanisms, fails to reproduce the post-peak softening behavior. Nonetheless, the models show reasonable accuracy in predicting the peak deviatoric stress, with absolute errors of 0.75%, 3.5%, and 1.05% for the MHMC, MHCS, and hypoplastic models, respectively. With respect to volumetric deformation, distinct differences are observed among the models. The MHCS model tends to overpredict the extent of dilation. Meanwhile, both the hypoplastic and MHMC models underpredict dilation.

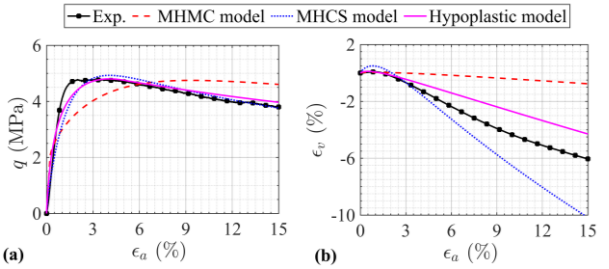

Figure 3. Plot of (a) deviatoric stress and (b) volumetric deformation with axial strain for cemented MHBS.

A comparative evaluation of model performance is conducted using box plots of absolute error in deviatoric stress and volumetric strain prediction, as depicted in Figure 4(a) and (b) respectively. The MHMC model exhibited the least accurate predictions, with medians for both deviatoric stress and volumetric strain errors significantly deviating from zero, along with noticeably wider IQRs, indicating high variability. In contrast, both the MHCS and hypoplastic models showed medians closer to zero with relatively narrow IQRs for deviatoric stress, reflecting better accuracy. However, the MHCS model demonstrated a wider IQR in volumetric strain compared to the hypoplastic model. This suggests that, among the three models, the hypoplastic model provides the most consistent and reliable prediction of both stress and volumetric deformation behavior.

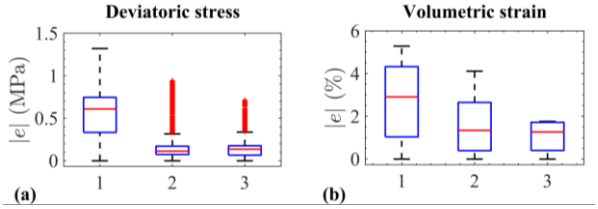

Figure 4. Comparison of absolute error in predicted (a) q and (b) ε_v by 1. MHMC model, 2. MHCS model and 3. Hypoplastic model for MHBS with cemented morphology.

The stress–strain and volumetric deformation behavior of MHBS with non-cementing hydrate pore morphology at a hydrate saturation of 40% is illustrated in Figure 5(a) and (b). Compared to specimens with cemented hydrate pore morphology, the non-cementing hydrate specimen exhibited a 1.8 fold less initial stiffness and a 1.6 fold lower peak deviatoric stress, clearly reflecting the reduced contribution of hydrates to the mechanical strength of the soil sediments when they occupy the pore space rather than forming cementation bonds at particle contacts. Additionally, the post-peak strain-softening behavior and volumetric dilation are notably less pronounced in the non-cemented specimens compared to the cemented MHBS.

Among the constitutive models examined, the hypoplastic model demonstrated strong agreement with the experimental data, capturing the stiffness and strength associated with the non-cemented morphology. This is achieved by adjusting the cementation coefficient α_h, allowing the model to flexibly transition between different hydrate pore morphologies without the need for extensive recalibration. In contrast, the MHCS model showed limitations in replicating the mechanical behavior of non-cemented hydrates. Although the MHCS model incorporates morphology-dependent effects through cementation and dilation functions (p'_{cc} and p'_{cd}), a recalibration of these, along with the shear modulus, is essential to represent changes in hydrate pore morphology accurately. This additional calibration requirement makes the model less adaptable when applied across varying hydrate formations. The MHMC model lacks explicit consideration of hydrate pore morphology. Its inability to distinguish between cemented and non-cemented morphologies results in reduced predictive accuracy. Therefore, its application in numerical modeling frameworks should be based on the thorough understanding of the expected hydrate formation.

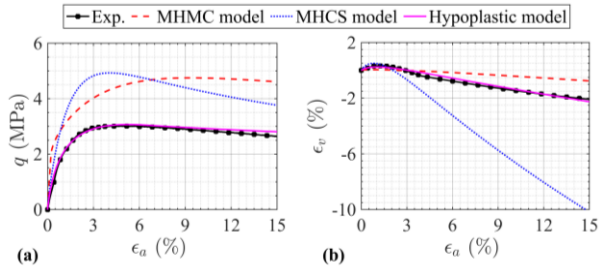

Figure 5. Plot of (a) deviatoric stress and (b) volumetric deformation with axial strain for non-cemented MHBS.

To further understand the effect of hydrate pore morphology on the stress–strain behavior and volumetric deformation of MHBS, a parametric analysis is conducted using the hypoplastic model by varying the cementation coefficient α_h from 0 to 1. A value of $\alpha_h = 0$ represents a purely pore-filled hydrate pore morphology. As the value of α_h increases, the morphology transitions from pore-filling to load-bearing and eventually purely cementing at $\alpha_h = 1$. The Figure 6(a) and (b) presents the stress-strain and volumetric strain for varying α_h for a hydrate saturation of 40%. As seen in the Figure 6, when $\alpha_h = 0$, regardless of 40% S_h the MHBS specimens exhibited mechanical behavior similar to that of the host sand (as shown in Figure 1(c) and (d)). This suggests that in a purely pore-filling hydrate pore morphology, hydrates do not significantly influence the strength or stiffness of the host material. However, as α_h increases from 0 to 1, both the peak deviatoric stress and the initial tangent stiffness rise, and the peak stress occurs at a lower axial strain (Figure 6(a)) typical to any cemented soil response (Kandasami et al. 2021). Additionally, the post-peak response transitions from strain hardening to softening. Moreover, as shown in Figure 6(b) volumetric deformation shifts from contraction to dilation as α_h approaches to 1. These changes can be attributed to the apparent cohesion induced by hydrate bonding as α_h increases, forming cementation. Upon shearing, these cementation bonds break, resulting in pronounced strain softening and dilation.

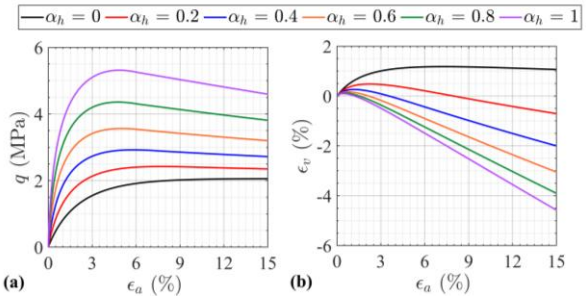

Figure 6. Plot of (a) deviatoric stress and (b) volumetric deformation with axial strain for different α_h values.

Based on the parametric analysis carried out using the hypoplastic model, peak deviatoric stress (q_{peak}) obtained for varying hydrate pore morphology (α_h) considering hydrate saturation ranging from 0 to 60% are shown in Figure 7(a). It can be observed that when $\alpha_h = 0$ (pore-filling morphology), there is minimal improvement in peak strength compared to the host sand, regardless of the hydrate saturation. However, as the cementation coefficient increases beyond 0.4, a noticeable nonlinear rise in q_{peak} is observed, with the increase being more significant at higher S_h values. For $S_h > 30\%$, the trend appears exponential, indicating that a small increase in α_h result in a large gain in strength. Similarly, Figure 7(b) shows the variation of peak dilation ($\psi_{peak} = \left(\frac{d\varepsilon_v}{d\varepsilon_q}\right)_{peak}$) with hydrate pore morphology across different hydrate saturations ($-\psi_{peak}$ in the Y-axis follows the sign convention adopted in this study, where dilation is negative and contraction is positive). For a given S_h, pore-filled hydrates exhibit minimal dilation. However, as α_h approaches 1, even at lower hydrate saturations like 20%, pronounced dilation is observed. These findings clearly demonstrate that hydrate pore morphology has a profound influence on the mechanical behavior of MHBS. Therefore, incorporating pore-scale hydrate distribution into geomechanical analysis is essential for accurately assessing the strength and deformation characteristics of HBS.

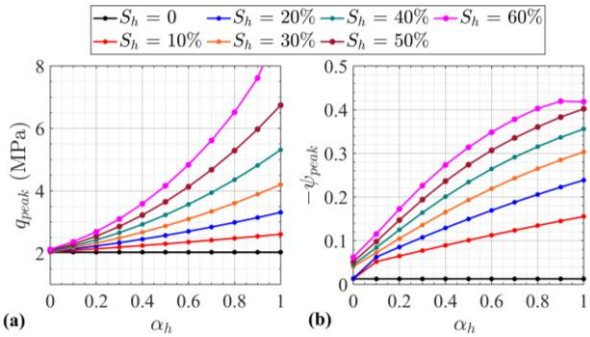

Figure 7. Plot of (a) peak deviatoric stress and (b) peak dilation with α_h values for different hydrate saturation.

4 CONCLUSIONS

The study presented a comprehensive experimental analysis and constitutive model prediction of the mechanical behavior of methane hydrate-bearing specimens under drained triaxial compression. The host and hydrate-bearing specimens are tested to evaluate the influence of hydrate saturation and morphology on stiffness, strength, and volumetric response. Experimental results demonstrated that hydrate presence

particularly in cemented morphology significantly enhances stiffness, peak deviatoric stress, and dilative response, while non-cemented morphology offers comparatively lower mechanical reinforcement. Three constitutive models are calibrated and evaluated against the experimental data: an elastic-perfectly plastic Mohr–Coulomb based model, the MHCS model, and a modified hypoplastic model. While all models captured peak strength and initial stiffness with reasonable accuracy for cemented morphology, notable differences emerged in their ability to represent post-peak and volumetric responses. The MHMC model lacked the ability to simulate strain softening and morphology-dependent behavior due to its simplified formulation. The MHCS model, although capable of capturing degradation and dilation trends, required recalibration for different hydrate pore morphologies. In contrast, the hypoplastic model demonstrated consistent accuracy across varying confinement pressures and morphologies, highlighting its robustness and adaptability. Furthermore, the parametric analysis conducted using the hypoplastic model indicates that hydrate pore morphology plays a dominant role in governing the geomechanical behavior of hydrate-bearing sediments. These results underscore the importance of incorporating morphology-sensitive mechanisms and degradation effects into constitutive formulations for realistic simulation of hydrate-bearing sediments. The insights gained here are valuable for selecting appropriate constitutive models for geomechanical analysis of hydrate-bearing sediments.

5 ACKNOWLEDGEMENTS

The first author would like to acknowledge the Prime Minister's Research Fellowship Scheme, INDIA, for the support during the research at IIT Madras.

6 REFERENCES

De La Fuente, M., Vaunat, J., and Marín-Moreno, H. 2020. A densification mechanism to model the mechanical effect of methane hydrates in sandy sediments. *International journal for numerical and analytical methods in geomechanics*, *44*(6), pp.782-802.

Gai, X., and Sánchez, M. 2017. A geomechanical model for gas hydrate-bearing sediments. *Environmental Geotechnics*, *4*(2), pp.143-156.

Hyodo, M., Yoneda, J., Yoshimoto, N., and Nakata, Y. 2013. Mechanical and dissociation properties of methane hydrate-bearing sand in deep seabed. *Soils and foundations*, *53*(2), pp.299-314.

Kandasami, R.K., Singh, S., and Murthy, T.G. 2021. Experimental investigations of the stress path dependence of weakly cemented sand. *Journal of Geotechnical and Geoenvironmental Engineering*, *147*(4), p.04021007.

Klar, A., Soga, K., and Ng, M.Y.A. 2010. Coupled deformation–flow analysis for methane hydrate extraction. *Geotechnique*, *60*(10), pp.765-776.

Lijith, K.P., Malagar, B.R., and Singh, D.N. 2019. A comprehensive review on the geomechanical properties of gas hydrate bearing sediments. *Marine and Petroleum Geology*, *104*, pp.270-285.

Liu, F., Kou, X.Y., Jiang, M.J., Xiong, J.H., and Wu, X.F. 2013. Triaxial shear strength of synthetic hydrate-bearing sediments. *Chinese Journal of Geotechnical Engineering*, *35*(8), pp.1565-1572.

Masui, A., Haneda, H., Ogata, Y., and Aoki, K. 2006, July. Triaxial Compression test on submarine sediment containing methane hydrate in deep sea off the coast off Japan. In *Proceedings of the 41st Annual Conference, Japanese Geotechnical Society*.

Miyazaki, K., Tenma, N., Aoki, K., and Yamaguchi, T. 2012. A nonlinear elastic model for triaxial compressive properties of artificial methane-hydrate-bearing sediment samples. *Energies*, *5*(10), pp.4057-4075.

Pinkert, S., and Grozic, J.L.H. 2014. Prediction of the mechanical response of hydrate-bearing sands. *Journal of Geophysical Research: Solid Earth*, *119*(6), pp.4695-4707.

Priest, J.A., Rees, E.V., and Clayton, C.R. 2009. Influence of gas hydrate morphology on the seismic velocities of sands. *Journal of geophysical research: solid earth*, *114*(B11).

Rao, M.S., Wani, S., and Kandasami, R.K. 2024, June. Experimental investigation and modeling of geomechanical behavior for methane hydrate-bearing sediments. In *ARMA US Rock Mechanics/Geomechanics Symposium* (p. D042S060R012). ARMA.

Rao, M.S., Wani, S., and Kandasami, R.K. 2025. Effect of Hydrate morphology on Geomechanical Behavior of Gas Hydrate Sediments. In *Geotechnical Frontiers 2025* (pp. 535-544).

Santamarina, J.C., Dai, S., Terzariol, M., Jang, J., Waite, W.F., Winters, W.J., Nagao, J., Yoneda, J., Konno, Y., Fujii, T., and Suzuki, K. 2015. Hydro-bio-geomechanical properties of hydrate-bearing sediments from Nankai Trough. *Marine and petroleum geology*, *66*, pp.434-450.

Sloan Jr, E.D., and Koh, C.A. 2007. Clathrate hydrates of natural gases. CRC press.

Uchida, S., Soga, K., and Yamamoto, K. 2012. Critical state soil constitutive model for methane hydrate soil. *Journal of geophysical research: solid earth*, *117*(B3).

Wani, S., Samala, R., Kandasami, R.K., and Chaudhuri, A. 2023. Positioning of horizontal well-bore in the hydrate reservoir using a custom developed coupled THMC solver. *Computers and Geotechnics*, 161, p.105618.

Wani, S., Kandasami, R.K., Kumar, R., and Wu, P. 2024. Disturbed State Concept-Based Model Incorporating Strain-Softening Behavior for Gas Hydrate Sediments. *Energy & Fuels*, *38*(10), pp.8712-8725.

Wani, S., and Kandasami, R.K. 2025. Identification and Extension of an Advanced Gas Hydrate Sediment Constitutive Model Using the Autocalibration Technique. *International Journal of Geomechanics*, *25*(5), p.04025050.

Wani, S., Kandasami, R.K., and Wu, W. 2025a. Hypoplastic model for gas hydrate-bearing sediments considering pore morphology. *Computers and Geotechnics*, *181*, p.107115.

Wani, S., Alipour, M.J., Kandasami, R.K., and Wu, W. 2025b. MS-IS Hypoplastic Model Considering Stiffness Degradation Under Cyclic Loading Conditions. *International Journal for Numerical and Analytical Methods in Geomechanics*, *49*(2), pp.776-793.

Wu, P., Li, Y., Liu, W., Liu, Y., Wang, D. and Song, Y. 2020. Microstructure evolution of hydrate-bearing sands during thermal dissociation and ensued impacts on the mechanical and seepage characteristics. *Journal of Geophysical Research: Solid Earth*, 125(5), p.e2019JB019103.

Zeng, Z., Kong, L., Zhao, Y., Sang, S., Niu, G., Liu, J., and Wang, N. 2023. Mechanical properties of gas hydrate-bearing sediments influenced by multiple factors: A comprehensive review of triaxial tests. *Energy & Fuels*, *37*(21), pp.16190-16220.

Zhang, X.H., Lu, X.B., Shi, Y.H., and Xia, Z. 2015. Study on the mechanical properties of hydrate-bearing silty clay. *Marine and Petroleum Geology*, *67*, pp.72-80.

Zhang, X., Lin, J., Lu, X., Liu, L., Liu, C., Li, M. and Su, Y., 2018. A hypoplastic model for gas hydrate-bearing sandy sediments. *International Journal for Numerical and Analytical Methods in Geomechanics*, *42*(7), pp.931-942.

Zhao, Y., Kong, L., Xu, R., Liu, J., and Sang, S. 2022. Strength behaviors of hydrate-bearing clayey-silty sediments with multiple factors. *Journal of Petroleum Science and Engineering*, *219*, p.111035.